In Situ Exploration of the Structural Transition during Morphology- and Efficiency-Conserving Halide Exchange on a Single Perovskite Nanocrystal

Karimata, Izuru
Tachikawa, Takashi

In Situ Exploration of the Structural Transition during Morphology- and Efficiency-Conserving Halide Exchange on a Single Perovskite Nanocrystal

Izuru Karimata and Takashi Tachikawa*

[*]   Dr. I. Karimata, Prof. T. Tachikawa
        Department of Chemistry, Graduate School of Science
        Kobe University
        1-1 Rokkodai-cho, Nada-ku, Kobe 657-8501 (Japan)
        Prof. T. Tachikawa
        Molecular Photoscience Research Center
        Kobe University
        1-1 Rokkodai-cho, Nada-ku, Kobe 657-8501 (Japan)
        Email: tachikawa@port.kobe-u.ac.jp

        Supporting information for this article is given via a link at the end of the document.

Abstract: Controlled fabrication of semiconductor nanostructures with unique physicochemical properties is vital for future technologies. In this study, transformation from red-emitting metal halide perovskite $CH_3NH_3PbI_3$ nanocrystals (NCs) to green-emitting $CH_3NH_3PbBr_3$ NCs was achieved without significant morphological changes and loss of photoluminescence (PL) efficiency via a controlled halide exchange reaction. In situ single-particle PL imaging along with detailed structural and elemental characterizations revealed that sudden cooperative transitions between two light-emitting states via intermediate dark states with >100 s durations during halide exchange originate from two distinct defect-mediated reconstruction processes with different activation energies (0.072 and 0.40 eV), leading to an isokinetic temperature of ~314 K, across a solid-state miscibility gap between the I- and Br-rich phases inside a single NC.

Introduction

Metal halide perovskites (e.g., MAPbI$_3$, MA = $CH_3NH_3^+$) have recently attracted much attention as light absorbers in photovoltaic cells[1] and as promising materials for optoelectronic applications including lasers[2] and light-emitting diodes.[3] One of the notable features of these materials is their structural diversity and softness. For example, the bandgap energy can be readily tuned by changing the composition of halide anions (Cl$^-$, Br$^-$, and I$^-$) to realize colorful and high-performance devices.[4] Meanwhile, it was reported that the metastable compositions and phases formed under operating conditions cause severe problems (e.g., current-voltage hysteresis behavior).[5] A precise control of nanostructures of perovskites is thus needed to manipulate their properties for improving the performance and for extending their potential applications.

Ion exchange reactions are useful for the fabrication of new types of nanocrystals (NCs) with unique structures and compositions that are difficult to access by direct synthetic methods.[6] For example, existing Cl$^-$ (or Br$^-$) ions within the crystal lattice of perovskite NCs are reversibly exchanged with diffusing incoming Br$^-$ (or I$^-$) at room temperature, resulting in mixed-halide perovskites while preserving their morphology.[7] However, the interplay of kinetics and thermodynamics of each reaction step governed by nanoscopic heterogeneities makes it difficult to control the nucleation and growth events occurring simultaneously over a wide range of time and length scales. Compared to all-inorganic perovskites (e.g., CsPbBr$_3$ and CsPbI$_3$), this issue is particularly pronounced for chemically unstable hybrid organic-inorganic perovskites.[8]

In situ microscopy observations with high temporal and spatial resolutions provide a mechanistic understanding of solid-state transformations on the nanoscale as well as guidance regarding the setting of the parameters that control the exchange reactions. In a pioneering work, Routzahn and Jain employed in situ single-particle photoluminescence (PL) imaging to obtain kinetic trajectories during cation exchange over individual CdSe NCs with Ag$^+$.[9] They proposed a stochastic reaction model that incorporates positive cooperativity between exchange events.[10] Recently, Wang et al. observed PL from individual CsPbBr$_3$ NCs generated during the halide exchange reaction of the parent CsPbCl$_3$ NCs with Br$^-$ (and vice versa) and found a strong dependence of the switching times of the changes in the PL intensity on the concentration of the substitutional halide ions.[11] Although previous studies have succeeded in providing some important insights into nanoscale transformation, the overall process is still not well understood. In particular, intermediate states present in the process and their structures have not been characterized at all because only either the reactant or the product NCs could be observed in the studies performed to date. Additionally, exciton and charge carrier dynamics that play a key role in any optoelectronic device are closely associated with the heterostructures that vary over time during ion exchange.[12]

In this study, we fully monitored the transformation from red-emitting MAPbI$_3$ NCs to green-emitting MAPbBr$_3$ NCs, while maintaining their morphology and PL efficiency by carrying out a precisely controlled halide exchange reaction, using a multi-wavelength single-particle PL imaging technique. It was found that the starting NCs are transformed to deficient MAPb(I$_{1-x}$Br$_x$)$_3$ NCs as non-emitting dark states with durations of more than 100 s, followed by a sudden transition to the light-emitting states with time constants of less than 10 s. Furthermore, combined with structural and elemental analyses, it was revealed that successive transitions between light-emitting and dark states are closely related to the solid-state miscibility between the I- and Br-rich phases in which defect-mediated reconstructions with different activation energies occur cooperatively.

Results and Discussion

Figure 1a shows the PL spectra of MAPbI$_3$ NCs with a mean size of ~90 nm during halide exchange with Br$^-$ using a custom-made flow reactor (Figures S1 and S2). Prior to the reaction, the MAPbI$_3$ NCs exhibited intense PL with a peak at approximately 770 nm and a quantum yield of ~3.6%. Initially, the controlled flow of *n*-octylammonium bromide (OA-Br) solution ([OA-Br] = 100 μM at a flow rate of 200 μL min^{-1}) caused a continuous peak shift from 770 nm to 620 nm accompanied by an initial increase which may be due to the passivation of surface defects, and a subsequent decrease in the PL intensity (red symbols in Figure 1b). However, PL peaks between 620 and 550 nm were not observed during and after the reaction, while a detectable peak appeared at approximately 550 nm after 40 min, and then became more intense over time and eventually shifted to 530 nm (green symbols in Figure 1b). The strong PL with a peak at approximately 530 nm is attributed to almost pure MAPbBr$_3$ NCs.[13] Overall, the observed peak shift from 770 nm to 530 nm indicates the conversion of MAPbI$_3$ NCs to MAPbBr$_3$ NCs with negligible loss (0.3%) of the PL quantum yield (Figure 1a). We note that a simple dropping or flow of the OA-Br solution at higher concentrations into the sample results in the decomposition of NCs.

Transmission electron microscopy (TEM) measurements showed that the cubic shape of the MAPbI$_3$ NCs was retained after 80 min of OA-Br flow while decreasing the size of the sample by ~40%, which is consistent with the difference in the lattice constants between MAPbI$_3$ and MAPbBr$_3$ (Figure S3). Energy dispersive X-ray spectroscopy (EDS) measurements using scanning TEM showed a Br/Pb ratio close to 3.0, also suggesting the formation of MAPbBr$_3$ (Figure S3). The optical absorption spectra during the reaction (Figure S4) revealed that the band edge continuously shifted from 755 nm to 525 nm, since the bandgap energies depend on the halide composition.[7a] Considering that MAPb(I$_{1-x}$Br$_x$)$_3$ NCs fully absorb excitation light at 405 nm, MAPb(I$_{1-x}$Br$_x$)$_3$ NCs with *x* in the range of 0.75–0.96, corresponding to the PL range between 620 and 550 nm, exhibit a much lower PL quantum yield (<0.2%) due to nonradiative deactivation. This interpretation is supported by the substantially shortened lifetimes due to the addition of the OA-Br solution (Figure S5).

A previous study has demonstrated the absence of PL during the halide exchange of MAPb(I$_{1-x}$Br$_x$)$_3$.[14] Pellet et al. have shown that MAPbI$_3$ microcrystals did not exhibit PL in the wavelength range between 535 and 609 nm during halide exchange until pure MAPbBr$_3$ was formed, while the X-ray diffraction (XRD) patterns continuously shifted.[14a] A similar trend was observed for MAPb(I$_{1-x}$Br$_x$)$_3$ synthesized directly using mixed-halide precursor solutions. Lehmann et al. showed that the bandgap of MAPb(I$_{1-x}$Br$_x$)$_3$ remains nearly constant in the halide composition range of 0.29 ≤ *x* ≤ 0.92, in addition to the absence of PL in the wavelength range between 717 and 556 nm.[15] They found that the XRD patterns of MAPb(I$_{1-x}$Br$_x$)$_3$ powders could be classified as those for I- and Br-rich phases due to the miscibility gap, resulting in a non-linear PL peak shift with increasing Br content. Moreover, for formamidinium lead mixed-halide perovskites FAPb(I$_{1-x}$Br$_x$)$_3$, the films with halide compositions in a certain range showed no PL emission and XRD patterns, indicating the formation of amorphous states.[16]

To confirm the structural transformation during the halide exchange reaction on NCs, XRD was performed. OA-Br solutions were flowed onto the MAPbI$_3$ NCs immobilized on the glass substrate and the flow was stopped at each reaction time, followed by gentle washing of the NCs with toluene. To prevent the decomposition of the NCs during X-ray measurements, a polystyrene solution was spin-coated on the NCs after washing.[17] Figure 2a shows the XRD patterns obtained in the 2θ range of 26–31°. The full range data are shown in Figure S6. Prior to the reaction, the MAPbI$_3$ NCs showed a (220) peak at 28.5°. As the reaction time increased, the (220) peak shifted toward higher angles. The substitution of larger I$^-$ ions (2.20 Å) by smaller Br$^-$ ions (1.96 Å) results in a shrinkage of the crystal lattice,[18] leading to an XRD peak shift toward higher angles. At a reaction time of 80 min, XRD peaks appeared at 30.1, 29.7, and 28.5°. The full range data for the reacted MAPbI$_3$ NCs are in agreement with the reported patterns of MAPbBr$_3$,[19] indicating that most MAPbI$_3$ NCs were almost completely converted to MAPbBr$_3$ NCs within 80 min, even though less than 5% of the initial intensity of the (220) peak at 28.5° remained. Considering that the XRD patterns were observed without any distinct features of the amorphous phase at all reaction times, it is concluded that the NCs almost maintained their crystallinity during the exchange reaction. At the reaction time of 10 min, it was found that a new peak located at a higher angle near 30° was observed in addition to the main peak of MAPb(I$_{1-x}$Br$_x$)$_3$ at 28.8°. The peak at a higher angle can be attributed to Br-rich perovskites with an almost cubic structure. This peak shifted toward smaller angles, and finally merged into the main peak of MAPb(I$_{1-x}$Br$_x$)$_3$ at 60 min.
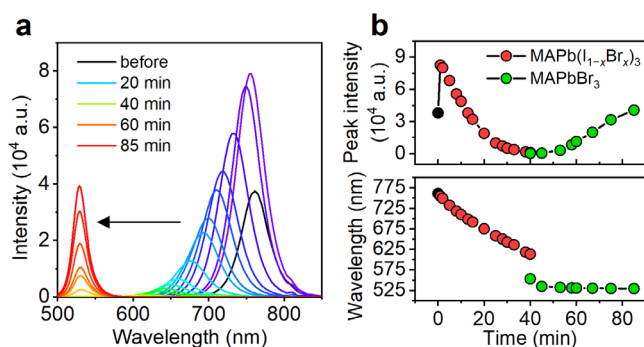
Figure 1. (a) Ensemble-averaged PL spectra during exchange on MAPbI$_3$ with Br$^-$ ions in solution. The excitation wavelength was 405 nm. (b) Temporal changes in the PL peak intensity and wavelength. Black symbols represent the results obtained for MAPbI$_3$.
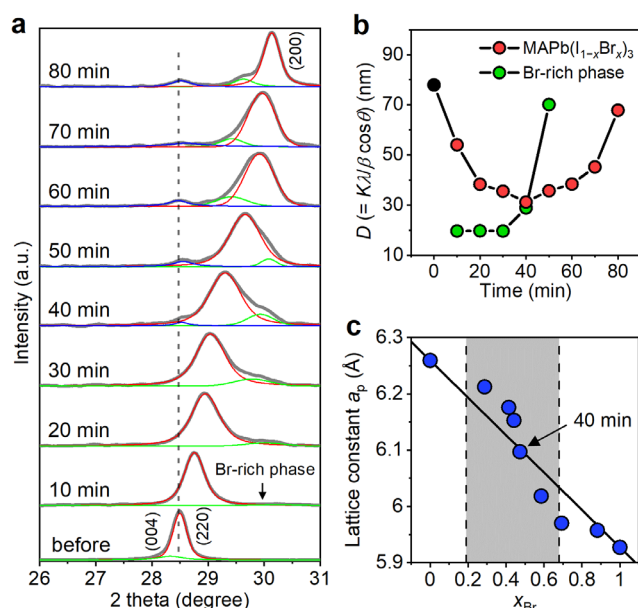
Figure 2. (a) Temporal changes in the XRD patterns (solid gray lines). Fitted Gaussian peaks are shown as solid red, green, and blue lines. (b) Temporal change in the domain size (D) of the MAPb($I_{1-x}Br_x)_3$ and Br-rich phase evaluated using the Scherrer equation. The black symbol represents the result obtained for MAPbI$_3$. (c) Relationship between a_p and x_{Br}. The gray region indicates the miscibility gap reported in Ref. 22

To obtain more insight into the structural transformation, the domain size (D) was evaluated using the Scherrer equation: $D = K\lambda/\beta\cos\theta$, where K is the Scherrer constant (0.9 was adopted here), λ is the X-ray wavelength (λ = 0.15418 nm, Cu Kα), and β is the full-width at half-maximum at the reflection angle (θ). As shown in Figure 2b, over 40 min, D gradually decreased from 78 nm, which is comparable to the sizes (90 ± 39 nm) of the NCs determined by TEM, to 31 nm, then increased to 68 nm at 80 min. Moreover, from the peak at a higher angle, D of the Br-rich phase was found to increase from 20 nm to 70 nm (Figure 2b, green symbols). Based on these results, it can be concluded that the successful substitution of I$^-$ in NCs by Br$^-$ through OA-Br flow initially caused a decrease in the size of I-rich MAPb($I_{1-x}Br_x)_3$ domains and led to the formation of a Br-rich phase on the surface. Further substitution led to an increase in the domain sizes of both MAPb($I_{1-x}Br_x)_3$ and Br-rich phases, and these two separated phases finally merged together.

The above-described structural transformation was also indicated by the significant shifts in the lattice constant. The pseudo-cubic lattice constant (a_p) of the MAPb($I_{1-x}Br_x)_3$ phase was determined from Rietveld analysis of the XRD patterns. As shown in Figure S7, the a_p value decreased linearly as a function of the reaction time up to 40 min, while a large deviation from the linearity was observed at 50 and 60 min. The deviations to smaller values indicate the mixing of MAPb($I_{1-x}Br_x)_3$ and the Br-rich phase, leading to the shrinkage of the lattice. We mention here that the lattice constants of MAPbI$_3$ NCs (a = 8.89 Å, c = 12.5 Å) and the final product after OA-Br flow for 80 min (a = 5.93 Å) matched well the lattice constants reported for tetragonal MAPbI$_3$ (a = 8.88 Å, c = 12.6 Å) and cubic MAPbBr$_3$ (a = 5.93 Å) single crystals, respectively.[20]

In a complete solid solution, the variation in the lattice constant with the concentration of the constituent element

follows Vegard's law, whereby lattice constants vary linearly with the concentration of the constituent elements. However, for MAPb($I_{1-x}Br_x)_3$ perovskites, the lattice constant varies non-linearly with the halide composition due to phase separation caused by miscibility. To reveal the range of the miscibility gap in the phase diagram, the halide compositions after the exchange reaction were determined by total reflection X-ray fluorescence (TXRF) analysis. TXRF measurements use an X-ray beam directed to a sample surface at a very small angle, allowing surface-sensitive analysis of a sample to depths as low as a few nanometers below the surface.[21] Figure 2c shows a plot of a_p as a function of the bromide molar fraction (x_{Br}). The black solid line shows a linear fitting obtained using only the two data points at x_{Br} = 0 and 1.0, and represents the Vegard's law-predicted a_p values. Interestingly, symmetry with respect to the data point at x_{Br} ~ 0.5 is observed, implying phase separation. The data points above (below) the Vegard's law-predicted line indicate the crystalline phase with larger (smaller) lattice constants in the two separated phases. Thus, the observed symmetrical dependence suggests that the initially formed MAPb($I_{1-x}Br_x)_3$ and the separated Br-rich phase are found in mixed states, the data points of which obey Vegard's law, followed by the growth of the MAPbBr$_3$ phase and the exclusion of the iodide phase from the inner region of the sample (Figure 3a). The data points deviating from Vegard's law are in agreement with the reported miscibility gap (gray region in Figure 2c).[22]
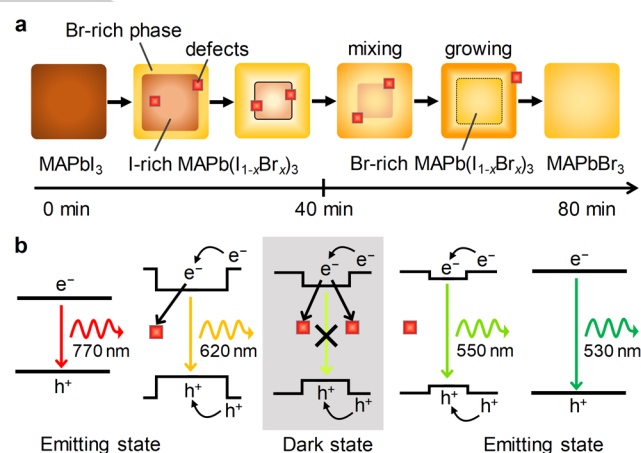
Figure 3. Schematic illustration of (a) structural changes and (b) charge carrier dynamics of NCs during the halide exchange reaction. e$^-$ and h$^+$ denote the photogenerated electrons and holes, respectively.

To clarify the discontinuous changes observed by ensemble-averaging optical and X-ray measurements and their effects on the charge carrier dynamics, single-particle PL observations were performed using a multi-wavelength imaging technique with two optical filters for selective detection based on the development of the PL spectra (Figure 4a and S8). As demonstrated in Figure 4b, the PL collected from dozens of reactant NCs (>593 nm range) gradually weakened with the progress of the exchange reaction under OA-Br flow, while PL from the products (510–560 nm range) appeared after a certain period of time. Meanwhile, individual NCs exhibited a sudden intensity drop and rise in PL, with the non-emitting period

reaching 100 s or greater (Figures 4c and S9). This finding suggests that intermediate(s) with low crystallinity and thus a weak luminescence (so-called dark state) were formed between the two light-emitting states. Almost the same trajectory was obtained with intermittent excitation light (Figure S10), excluding the involvement of the light-induced degradation or halide phase segregation as well as sample heating.[23]

To quantitatively characterize the transition processes, the intensity trajectories were tentatively fitted with the Boltzmann sigmoidal equation:

$$I(t) = I_{\text{initial}} + \frac{I_{\text{final}} - I_{\text{initial}}}{1 + \exp\{(t - t_{\text{wait}})/\tau_{\text{switch}}\}} \quad (1)$$

where I_{initial} and I_{final} are the initial and final values, respectively. The parameter t_{wait} is the center (the inflection point) of the dependence and was used to determine the characteristic time required for structural changes, and τ_{switch} is the width of the transition from the light-emitting state to the dark state (and vice versa) (Figure 4c).
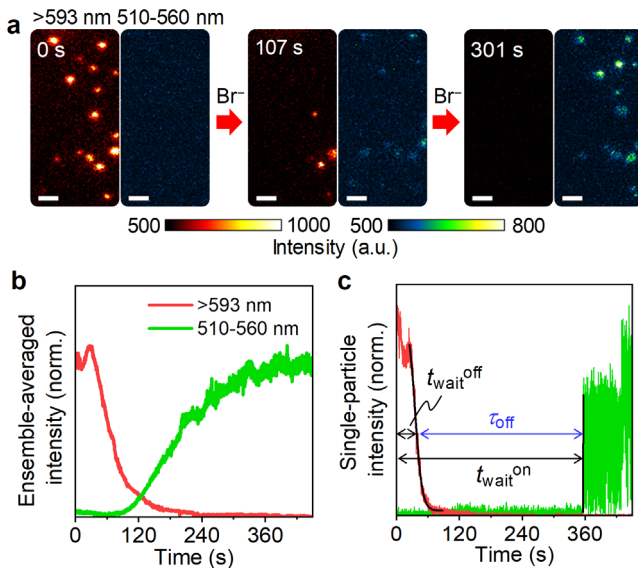

Figure 4. (a) Dual channel single-particle PL images during halide exchange reaction acquired under 405 nm laser irradiation (5 mW cm^{-2}). The scale bars are 2 µm. Temporal changes in (b) ensemble-averaged and (c) single-particle PL intensities.

As shown in Figure 5a, the histograms of $t_{\text{wait}}^{\text{off/on}}$ for PL turn-off/on events were distributed over a wide range of times, but unfortunately masked the inherent static and dynamic disorder. To characterize the dark state, therefore, the dark time (τ_{dark}) was determined as the difference between $t_{\text{wait}}^{\text{off}}$ and $t_{\text{wait}}^{\text{on}}$ for individual NCs (Figure 5b). If the transition from the dark state to the light-emitting state has a constant probability of occurrence, exponential distribution of the duration is expected. However, the histogram of τ_{dark} has a peak, suggesting that the transition is not a simple first-order reaction that is determined by a single time constant. To reveal the hidden relationship between the kinetic and structural parameters, correlated PL and field emission-scanning electron microscopy (FE-SEM) measurements were carried out (Figure S11). Here, we assumed that τ_{dark} is the time required for the adsorbed Br$^-$ ions

to diffuse and replace most I$^-$ ions inside the NC. In fact, much shorter τ_{dark} values were obtained for the MAPbI$_3$ NCs with smaller sizes (~7 nm) (Figure S12). The diffusion time (t_{diff}) is known to be proportional to the square of the diffusion length, $t_{\text{diff}} \approx r^2/\alpha D_{\text{diff}}$, where r is the particle radius, α is the geometric factor, and D_{diff} is the diffusion coefficient.[24] As demonstrated in the inset of Figure 5b, a positive correlation was observed between τ_{dark} and r^2. From the slope and α of 0.15 for a spherical particle,[24] D_{diff} was calculated as 3.1×10^{-12} cm^2 s^{-1}, which is close to that (~10^{-12} cm^2 s^{-1}) reported for iodine vacancies (V$_\text{I}^+$).[25] This result implies that charge carrier dynamics on the pico- to nanosecond time scale are coupled with slow ion (vacancy) dynamics on the millisecond to second time scale.

On the other hand, the histograms of $\tau_{\text{switch}}^{\text{off/on}}$ for the PL turn-off/on processes exhibit an exponential distribution (Figure 4c). From the single-exponential fits, the mean values ($<\tau_{\text{switch}}^{\text{off/on}}>$) were determined to be 2.6 and 7.4 s for the turn-off and turn-on processes, respectively. These time constants are much longer than that (few 100 ms) reported for cooperative transition from CdSe (3.5 nm in diameter) to Ag$_2$Se.[9] Furthermore, from the Arrhenius plots of these parameters (Figures 5d and S13), the activation energies (E_a) were evaluated as 0.072 ± 0.044 and 0.40 ± 0.16 eV for $\tau_{\text{switch}}^{\text{off}}$ and $\tau_{\text{switch}}^{\text{on}}$, respectively, suggesting that their origins are different. Moreover, an E_a value (0.52 ± 0.05 eV) close to the latter was obtained for τ_{dark} (Figure S13).
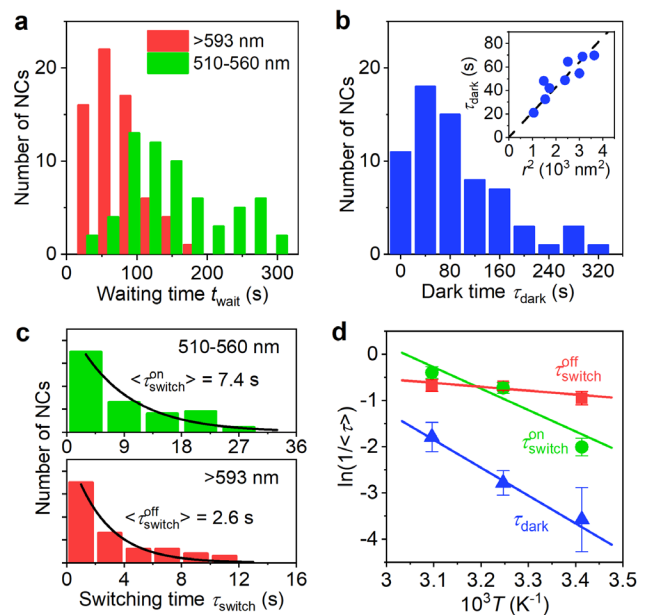
Figure 5. (a) Histograms of $t_{\text{wait}}^{\text{off}}$ (red bars) and $t_{\text{wait}}^{\text{on}}$ (green bars). (a) Histogram of τ_{dark}. The solid line indicates the best fit obtained based on eq. 2. The inset shows the relationship between τ_{dark} and r^2. (c) Distributions of $\tau_{\text{switch}}^{\text{off}}$ (red) and $\tau_{\text{switch}}^{\text{on}}$ (green). (d) Arrhenius plots for $\tau_{\text{switch}}^{\text{off}}$ (red), $\tau_{\text{switch}}^{\text{on}}$ (green), and τ_{dark} (blue).

Based on these findings, we introduce a new perspective related to charge carrier dynamics into the consideration of the ion exchange reaction mechanism, as illustrated in Figure 3b. Prior to the reaction, PL from MAPbI$_3$ was observed at approximately 770 nm. As the exchange reaction proceeds, Br-rich shells are formed on the surface, and the I-rich core inside the crystal is partially exchanged with Br$^-$ ions. In such a

structure, PL emission occurs only from the I-rich perovskite with a smaller band gap due to the interfacial charge transfer.[12] Furthermore, numerous defects are generated during the exchange reaction, as suggested by the decreased PL intensity, shortened PL lifetime, and slightly weakened and broadened XRD peaks. As the reaction proceeds, the density of internal defects that may be located at the grain boundaries increases accordingly, resulting in the quenching of PL, and thus, the transition to the dark state. As long as the defects exist, the dark state will persist. However, as the reaction proceeds, the defects are gradually reduced by the incorporation of Br⁻ into the crystal, and at the point in time when one or a few remaining defects that act as effective charge traps inside the NCs disappear, the PL from MAPbBr$_3$ suddenly increases.

These transitions are a highly cooperative process that is controlled by the change in the Gibbs free energy (G). When the free energy is plotted as a function of composition (Figure S14), the region lying within the inflection points of the curve ($\partial^2 G/\partial x_{Br}^2 = 0$) is intrinsically unstable. The composition within this so-termed spinodal region can separate the system into two phases without a thermodynamic barrier. Importantly, this phase separation is triggered by microscopic fluctuations in composition and is solely diffusion-controlled (so-called uphill diffusion).[26] As mentioned above, MAPb(I$_{1-x}$Br$_x$)$_3$ samples synthesized from stoichiometric mixtures of MAI, MABr, and PbI in solution did not show PL in the range of 717–556 nm because of the miscibility gap of $0.29 \leq x \leq 0.92$.[15] It is evident that phase separation occurs in our system, but dynamic equilibrium between the mixed and separated phases during the exchange reaction may result in detectable PL up to 620 nm ($x \sim 0.75$). This may provide a partial answer as to why the observed transitions with $\tau_{switch}^{off/on}$ are very slow (Figure 5c).

Finally, we discuss the reconstruction process based on the obtained thermodynamic parameters. The E_a values experimentally determined from the current-voltage curves of the MAPbI$_3$- and MAPbBr$_3$-based solar cells are 0.33 eV and 0.17 eV, respectively, which are in excellent agreement with those for the migration of V$_I^+$ (0.28 eV) and the bromine vacancy (V$_{Br}^+$) (0.22 eV) predicted from first-principles calculations.[27] The tendency (i.e., E_a on Br-rich NCs > E_a on I-rich NCs) observed herein is opposite to this trend, and hence cannot be simply explained in terms of the diffusibility of halide vacancies that act as charge traps. As a different type of mobile defects, interstitial halide ions have been proposed.[28] The energy barrier for the hopping of the iodine interstitial (I$_i^-$) was reported to be 0.12 eV, which is smaller than that (0.17 eV) of V$_I^+$.[29] It is presumed that I⁻ ions are pushed out by excess Br⁻ ions on the surface and trapped at the interstitial sites. These mobile I⁻ ions inside the NC capture the photogenerated holes, leading to PL quenching.

Another possible explanation is based on the crystallinity of the NCs. Xing et al. reported that the lower E_a (0.27 eV) for the small-grain film (~300 nm) compared to that (0.50 eV) for the large-grain film is probably due to the higher density of the grain boundaries that provide a higher likelihood of forming ion migration channels.[30] The lower E_a for the PL turn-off process on I-rich NCs may originate from their deficient structures with relatively poor crystallinity, while greater energy is required in the PL turn-on process on Br-rich NCs for the overall reconstruction to well-crystallized MAPbBr$_3$.

Importantly, Figure 5d reveals that the isokinetic temperature (T_{iso}) for τ_{switch} is approximately 313.5 K (40.4 °C), which is lower

than the tetragonal-to-cubic phase transition temperature (327.4 K) of MAPbI$_3$.[31] T_{iso} is a fundamentally important parameter for the optimization of the process design, and its existence indicates the compensation of enthalpy and entropy. According to the multi-excitation entropy model, when a transition is associated with a fluctuation that involves a large number of excitations of phonons (i.e., a large entropy), a large activation barrier is overcome.[32] This point of view appears to be reasonable because ion migration accompanied by reconstruction is strongly associated with the required number of phonon modes involving octahedral tilting and molecular reorientation. It has been reported that halide anions are bound to NH$_3^+$ in the MA, and lighter halides result in a smaller cavity that raises the frequencies of the molecular modes.[33] This mechanism may explain in part why the PL turn-on process on Br-rich NCs exhibits a higher prefactor in the Arrhenius plots (Figure 5d).

Conclusion

This study clarifies the fundamental aspects underlying the structural transformation of mixed-halide perovskite NCs during halide exchange. Because of the miscibility gap, individual MAPb(I$_{1-x}$Br$_x$)$_3$ NCs partly separate into two phases accompanying the formation of core–shell structures with significant defects, resulting in non-emitting dark states. After more than 100 s of inaction related to the intraparticle diffusion of ions (vacancies), a cooperative transition to the light-emitting state suddenly occurs with a time constant of ~7 s. Single-particle analysis further revealed that the transitions between the two states are closely related to defect-mediated structural changes with different activation energies (0.072 and 0.40 eV), leading to an isokinetic temperature of ~314 K. Our single-particle approach for controlling and evaluating the rate-limiting processes of ion exchange on nanostructures will help to improve device performance and will open new avenues for extending the applications of halide perovskite NCs.

Acknowledgements

[1]   a) M. A. Green, A. Ho-Baillie, H. J. Snaith, *Nat. Photonics* **2014**, *8*, 506-514; b) A. K. Jena, A. Kulkarni, T. Miyasaka, *Chem. Rev.* **2019**, *119*, 3036-3103.

[2]   H. Zhu, Y. Fu, F. Meng, X. Wu, Z. Gong, Q. Ding, M. V. Gustafsson, M. T. Trinh, S. Jin, X. Y. Zhu, *Nat. Mater.* **2015**, *14*, 636-642.

[3]   Z.-K. Tan, R. S. Moghaddam, M. L. Lai, P. Docampo, R. Higler, F. Deschler, M. Price, A. Sadhanala, L. M. Pazos, D. Credgington, F. Hanusch, T. Bein, H. J. Snaith, R. H. Friend, *Nat. Nanotechnol.* **2014**, *9*, 687-692.

[4]   a) J. H. Noh, S. H. Im, J. H. Heo, T. N. Mandal, S. I. Seok, *Nano Lett.* **2013**, *13*, 1764-1769; b) D. P. McMeekin, G. Sadoughi, W. Rehman, G. E. Eperon, M. Saliba, M. T. Hoerantner, A. Haghighirad, N. Sakai, L. Korte, B. Rech,

M. B. Johnston, L. M. Herz, H. J. Snaith, *Science* **2016**, *351*, 151-155.

[5]   H. J. Snaith, A. Abate, J. M. Ball, G. E. Eperon, T. Leijtens, N. K. Noel, S. D. Stranks, J. T.-W. Wang, K. Wojciechowski, W. Zhang, *J. Phys. Chem. Lett.* **2014**, *5*, 1511-1515.

[6]   L. De Trizio, L. Manna, *Chem. Rev.* **2016**, *116*, 10852-10887.

[7]   a) D. M. Jang, K. Park, D. H. Kim, J. Park, F. Shojaei, H. S. Kang, J.-P. Ahn, J. W. Lee, J. K. Song, *Nano Lett.* **2015**, *15*, 5191-5199; b) G. Nedelcu, L. Protesescu, S. Yakunin, M. I. Bodnarchuk, M. J. Grotevent, M. V. Kovalenko, *Nano Lett.* **2015**, *15*, 5635-5640; c) Q. A. Akkerman, V. D'Innocenzo, S. Accornero, A. Scarpellini, A. Petrozza, M. Prato, L. Manna, *J. Am. Chem. Soc.* **2015**, *137*, 10276-10281; d) Y. Fu, H. Zhu, C. C. Stoumpos, Q. Ding, J. Wang, M. G. Kanatzidis, X. Zhu, S. Jin, *ACS Nano* **2016**, *10*, 7963-7972; e) D. Pan, Y. Fu, J. Chen, K. J. Czech, J. C. Wright, S. Jin, *Nano Lett.* **2018**, *18*, 1807-1813.

[8]   Y. Zhou, Y. Zhao, *Energy Environ. Sci.* **2019**, *12*, 1495-1511.

[9]   A. L. Routzahn, P. K. Jain, *Nano Lett.* **2014**, *14*, 987-992.

[10]   S. L. White, J. G. Smith, M. Behl, P. K. Jain, *Nat. Commun.* **2013**, *4*, 3933/3931-3933/3938.

[11]   D. Wang, J. Cavin, B. Yin, A. S. Thind, A. Y. Borisevich, R. Mishra, B. Sadtler, *J. Phys. Chem. Lett.* **2020**, *11*, 952-959.

[12]   a) I. Karimata, Y. Kobori, T. Tachikawa, *J. Phys. Chem. Lett.* **2017**, *8*, 1724-1728; b) I. Karimata, K. Ohta, Y. Kobori, T. Tachikawa, *ACS Appl. Mater. Interfaces* **2018**, *10*, 37057-37066.

[13]   T. Tachikawa, I. Karimata, Y. Kobori, *J. Phys. Chem. Lett.* **2015**, *6*, 3195-3201.

[14]   a) N. Pellet, J. Teuscher, J. Maier, M. Gratzel, *Chem. Mater.* **2015**, *27*, 2181-2188; b) A. B. Wong, M. Lai, S. W. Eaton, Y. Yu, E. Lin, L. Dou, A. Fu, P. Yang, *Nano Lett.* **2015**, *15*, 5519-5524.

[15]   F. Lehmann, A. Franz, D. M. Toebbens, S. Levcenco, T. Unold, A. Taubert, S. Schorr, *RSC Adv.* **2019**, *9*, 11151-11159.

[16]   W. Rehman, R. L. Milot, G. E. Eperon, C. Wehrenfennig, J. L. Boland, H. J. Snaith, M. B. Johnston, L. M. Herz, *Adv. Mater.* **2015**, *27*, 7938-7944.

[17]   X. Wang, X. Lian, Z. Zhang, H. Gao, *ACS Energy Lett.* **2019**, *4*, 1446-1454.

[18]   R. D. Shannon, *Acta Crystallogr., Sect. A* **1976**, *A32*, 751-767.

[19]   a) C. Li, J. Wei, M. Sato, H. Koike, Z.-Z. Xie, Y.-Q. Li, K. Kanai, S. Kera, N. Ueno, J.-X. Tang, *ACS Appl. Mater. Interfaces* **2016**, *8*, 11526-11531; b) P. Sadhukhan, S. Kundu, A. Roy, A. Ray, P. Maji, H. Dutta, S. K. Pradhan, S. Das, *Cryst. Growth Des.* **2018**, *18*, 3428-3432.

[20]   P. K. Nayak, D. T. Moore, B. Wenger, S. Nayak, A. A. Haghighirad, A. Fineberg, N. K. Noel, O. G. Reid, G. Rumbles, P. Kukura, K. A. Vincent, H. J. Snaith, *Nat. Commun.* **2016**, *7*, 13303.

[21]   P. Wobrauschek, *X-Ray Spectrom.* **2007**, *36*, 289-300.

[22]   F. Brivio, C. Caetano, A. Walsh, *J. Phys. Chem. Lett.* **2016**, *7*, 1083-1087.

[23]   E. T. Hoke, D. J. Slotcavage, E. R. Dohner, A. R. Bowring, H. I. Karunadasa, M. D. McGehee, *Chem. Sci.* **2015**, *6*, 613-617.

[24]   C. Zhu, R. E. Usiskin, Y. Yu, J. Maier, *Science* **2017**, *358*, 1400.

[25]   a) G. Richardson, S. E. J. O'Kane, R. G. Niemann, T. A. Peltola, J. M. Foster, P. J. Cameron, A. B. Walker, *Energy Environ. Sci.* **2016**, *9*, 1476-1485; b) C. Eames, J. M. Frost, P. R. F. Barnes, B. C. O'Regan, A. Walsh, M. S. Islam, *Nat. Commun.* **2015**, *6*, 7497.

[26]   A. Paul, T. Laurila, S. Divinski, *Handbook of Solid State Diffusion, Vol. 1*, Elsevier, United States, **2017**.

[27]   S. Meloni, T. Moehl, W. Tress, M. Franckevicius, M. Saliba, Y. H. Lee, P. Gao, M. K. Nazeeruddin, S. M. Zakeeruddin, U. Rothlisberger, M. Graetzel, *Nat. Commun.* **2016**, *7*, 10334.

[28]   a) Y. Zhao, C. Liang, H. Zhang, D. Li, D. Tian, G. Li, X. Jing, W. Zhang, W. Xiao, Q. Liu, F. Zhang, Z. He, *Energy Environ. Sci.* **2015**, *8*, 1256-1260; b) X. Wen, A. Ho-Baillie, S. Huang, R. Sheng, S. Chen, H.-c. Ko, M. A. Green, *Nano Lett.* **2015**, *15*, 4644-4649.

[29]   D. Meggiolaro, E. Mosconi, F. De Angelis, *ACS Energy Lett.* **2019**, *4*, 779-785.

[30]   J. Xing, Q. Wang, Q. Dong, Y. Yuan, Y. Fang, J. Huang, *Phys. Chem. Chem. Phys.* **2016**, *18*, 30484-30490.

[31]   T. Baikie, Y. Fang, J. M. Kadro, M. Schreyer, F. Wei, S. G. Mhaisalkar, M. Graetzel, T. J. White, *J. Mater. Chem. A* **2013**, *1*, 5628-5641.

[32]   Yelon, Movaghar, *Phys Rev Lett* **1990**, *65*, 618-620.

[33]   R. G. Niemann, A. G. Kontos, D. Palles, E. I. Kamitsos, A. Kaltzoglou, F. Brivio, P. Falaras, P. J. Cameron, *J. Phys. Chem. C* **2016**, *120*, 2509-2519.

Entry for the Table of Contents
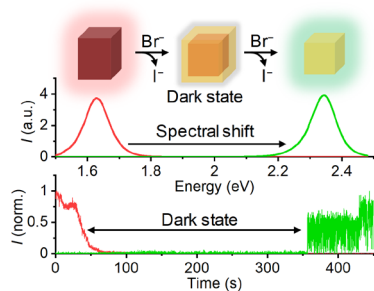
In situ single-particle photoluminescence imaging revealed that sudden cooperative transition from green-emitting $CH_3NH_3PbI_3$ perovskite nanocrystals to red-emitting $CH_3NH_3PbBr_3$ while maintaining their morphology and emission efficiency during halide exchange. The transformation proceeds via intermediate dark states with >100 s durations and originates from two distinct defect-mediated processes with different activation energies.